ARTICLE

Metal Oxide Microrings with Femtoliter Capacity for Raman Microspectroscopy

Ivano Alessandri* and Laura E. Depero

INSTM and Chemistry for Technologies Laboratory, University of Brescia, via Branze 38, 25123 Brescia, Italy

ABSTRACT A simple strategy, based on ultrafast heating of polystyrene microspheres infiltrated with a zinc acetate solution, is employed here for preparing ZnO microcontainers with femtoliter capacity. Their potential exploitation in micro-Raman assays for basic studies in bio- and nanotechnology is tested in different proof-of-concept experiments concerning the in situ analysis of L-glutathione crystals and gold–yeast cytochrome *c* bioconjugates. The ZnO microcontainers are also used as scaffolds for atomic layer deposition of TiO_2 overlayers with a fine-tuning of thickness and morphology. The resulting ZnO/TiO_2 heterostructures are tested in different photocatalytic experiments involving degradation and laser-induced conversion of methylene blue.

KEYWORDS: microrings • Raman • ZnO • TiO_2 • ALD

1. INTRODUCTION

Advances in the fabrication of containers with ultrasmall capacities (from femto- to attoliters) promise to bring about important breakthroughs in many fields of chemistry and nano(bio)technology (1). Reduced volumes and spatial compartmentalization at micro- and nanolength scales are essential prerequisites for investigating important processes, including enzymatic reactions, drug activity, stem-cell differentiation, etc. In particular, interactions occurring at biomolecule–inorganic interfaces are of great interest for tissue engineering, biomaterials, neural-based circuits, and bionic devices. Applications of microwells and -containers can also be extended to more basic topics, such as the synthesis, growth, and reactivity of either inorganic nanocrystals (2) or proteins (3) in confined spaces, and they may be valid experimental platforms for combinatorial chemistry approaches (4).

Microcontainers have been prepared in several ways, which may include different combinations of hard and soft lithography (5) and the use of focused-ion-beam nanofabrication or contact printing (6). An inexpensive alternative to conventional techniques could by represented by nanosphere lithography (7), which has often been employed for the production of micro- and nanorings. Yan and Goedel pioneered the use of colloidal crystal templates to achieve differently sized nanorings (8). Yang and co-workers proposed a general approach based on the combination of nanosphere lithography and reactive ion etching (RIE) for preparing nanoring arrays of a large variety of materials (9). Adapting ring-shaped structures to operate as microcontainers could foster promising solutions for most of the previously mentioned applications. In particular, important advantages could be obtained by expanding the compositional range of materials employed as microcontainers (which is usually restricted to polymers or silica) to functional transition-metal oxides such as TiO_2 and ZnO. This might allow the achievement of accurate experimental model systems that can be useful either for developing more efficient photocatalysts (10) or for advancing the understanding of interactions between inorganic interfaces and biochemical species (11).

At the same time, the upsurge of these researches goes along with the development of useful strategies for a direct, in situ monitoring of the chemical and physical events under investigation. Fluorescence spectroscopy has been intensively employed in many biochemical assays, e.g., to map the activity of enzymes entrapped in microfabricated arrays of femtoliter chambers (1, 12). Synchrotron radiation techniques, already employed for a detailed investigation of spatial heterogeneities in solid catalysts (13), can be helpful also for characterizing reactions in microcontainers. However, typical experiments are carried out under a controlled environment and high vacuum, i.e., under working conditions that are significantly different from those that take place in real processes. In this context, micro-Raman spectroscopy can represent a powerful tool for characterizing microcontainers and their content, as well as for monitoring reactions and interfacial processes. On the one hand, Raman spectroscopy may provide insightful information on the structural (with particular sensitivity to local distortions and residual stresses) and electronic properties of a sample with both high spatial (1 μm) and spectral (less than 1 cm^{-1}/pixel) resolution. In addition, the coupling of a Raman spectrophotometer to an optical microscope allows for a direct inspection of specific regions of the sample, which is a particularly suitable option in the case of microwell-based assays. A further key advantage comes from the design of microcontainers that can serve as active substrates for surface-enhanced Raman spectroscopy (SERS). This technique takes advantage of an extrasensitivity due to the strong local electromagnetic field developed upon interaction of the exciting laser with surface plasmons of roughened

* E-mail: ivano.alessandri@ing.unibs.it.

Received for review December 17, 2009 and accepted February 1, 2010

DOI: 10.1021/am900904k

Published on Web 02/08/2010

or nanostructured metals such as silver, gold, and copper (14). In some cases, in addition to the electromagnetic enhancement, charge transfer between molecular species adsorbed on the metal surface and the metal itself provides a further "chemical" enhancement, which may be exploited to push the detection limit down to the single molecule (15).

All of these potential advantages stimulated most of the recent research in producing microwells analyzable by micro-Raman spectroscopy. For example, Bhuvana and Kulkarni proposed SERS-active femtoliter cups made of silver obtained by pulsed-laser deposition (16). Zamuner et al. fabricated microwell arrays on the distal face of an etched optical fiber bundle and tested these systems for SERS detection of benzenethiol monolayers, opening promising perspectives for the sensing and imaging of bioanalytes (17). Ko and Tsukruk used nanocanal arrays with inner walls decorated by gold nanoparticles (Au NPs) as 3D SERS substrates (18). The focalization of a probing laser through a microscope can allow for a full exploitation of microcontainers as platforms for an in situ characterization of laser-induced reactions or processes. Moreover, SERS-active microwells might extend the use of plasmonic heating effects to a number of intriguing applications (19–21).

Here we reported a rapid and versatile route for generating ZnO-based microwells that may be easily engineered with metal nanoparticles or other metal oxides to serve as both SERS-active femtoliter containers and model systems for photocatalytic interfaces and laser-induced reactions. These functions were tested through a series of proof-of-concept experiments concerning (1) monitoring of a tripeptide crystallization, (2) detection and structural analysis of a heme protein, and (3) photodegradation and laser-induced photoconversion of a model azo dye.

2. EXPERIMENTAL SECTION

Preparation of ZnO and ZnO/TiO_2 Microrings. The ZnO microrings were prepared as follows. A 1 wt % suspension of monodisperse polystyrene (PS) beads (diameter 5.46 ± 0.12 μm; Microparticles GmbH) in deionized water was deposited onto glass or Si(100) substrates that had been previously ozone−UV-cleaned for 5 min. After drying, random monolayered networks of PS were formed. The interconnectivity and mechanical stability of the PS chains were improved by heating the substrates at 125 °C for 30 s. The substrates were dipped for 1 h into a 0.05 M zinc acetate/ethanol solution. After drying, the substrates were put onto the hot plate of a HFS91 heating stage (Linkam Scientific Instruments) at 450 °C for 10 min and then quenched in air at room temperature. If requested by subsequent experiments, the size of the ZnO crystallite can be improved by prolonging the annealing procedure at 450 °C for several hours. The samples shown in Figure 1 were obtained upon annealing for 1 h. Larger ZnO crystals may be obtained faster (1 h was enough) by annealing at 600 °C. Some of these ZnO microrings were used as scaffolds to prepare ZnO/TiO_2 core/shell heterostructures. The 50-nm-thick TiO_2 layer was deposited in a Savannah 100 atomic layer deposition (ALD) flow reactor (Cambridge Nanotech Inc.), using tetrakis(dimethylamido)titanium (TDMAT; Aldrich) as the titanium source and water as the oxygen source. The deposition temperature and pressure were respectively 90 °C and 0.5 Torr. TDMAT (99.999%) and H_2O were evaporated from stainless steel reservoirs held respectively at 80 °C and at room temperature and led into the reactor through solenoid valves. Nitrogen was used as a precursor carrier and purge gas. The processing cycle consisted of a TDMAT pulse of 0.1 s, a 5 s purge pulse of nitrogen, a 0.1 s pulse of water vapor, and a 5 s pulse of nitrogen. The deposition rate was 0.0667 nm per cycle. The as-deposited layers were annealed at 450 °C for 3 h. The thickness of TiO_2 was evaluated on the basis of the procedure described in our previous work (10).

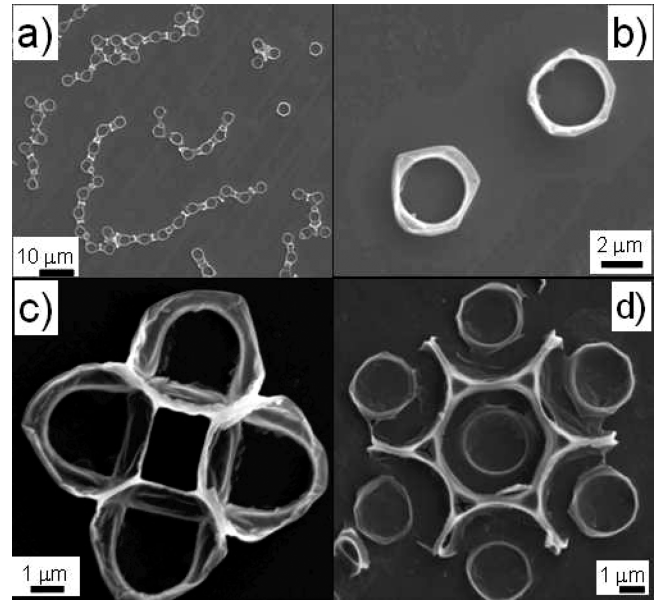

FIGURE 1. SEM images of the ZnO microrings generated by fast heating of the precursor-infiltrated PS templates. (a) Low magnification showing necklace structures, multimers, and single rings (a lower magnification image is reported in Figure S2 in the Supporting Information). (b) High-magnification images of isolated, "unchained" rings (see the text for details). (c and d) Examples of complex multimeric structures coming from the rapid decomposition of PS assemblies.

Structural and Microstructural Characterization. 2D X-ray diffraction (XRD) was performed using a D-max rapid diffractometer (Rigaku; incidence 10°, Cu Kα radiation source, operation voltage 40 kV, current 40 mA). The X-ray beam was collimated with a pinhole (diameter 300 μm), and the regions of interest were selected by a digital camera focused onto the specimen. SEM images were acquired by an EVO 40 (Leo-Karl Zeiss SMT) instrument. The average thickness of the microrings was evaluated by noncontact atomic force microscopy (AFM) using a JEOL scanning probe microscope, equipped with a conventional piezoscanner (maximum xy movement = 28 μm; maximum z movement = 4 μm).

Proof-of-Concept Experiments. All of the micro-Raman measurements were acquired by means of a Labram HR spectrophotometer (Jobin-Yvon/Horiba), equipped with a He−Ne laser (λ = 632.8 nm) source focused through the objectives (Olympus) of an optical microscope. The micro-Raman monitoring of L-glutathione crystallization into ZnO microrings was carried out by dropping 1 μL of a saturated water solution of reduced L-glutathione (Sigma-Aldrich) onto a ZnO microring substrate. The precipitate was then heated at 115 °C for 4 h. Raman spectra were acquired by focusing the laser onto the crystals entrapped in the microrings. The spectra were collected for 60 s using a 50× objective [numerical aperture (NA) 0.75].

For SERS detection of yeast cytochrome *c* (YCc), 3 μL of a 100 μM solution of YCc from *Saccharomyces cerevisiae* (MW 12 588 Da) in phosphate-buffered saline was conjugated to colloidal Au NPs (average size 15 nm, prepared by a citrate method as described in ref 21) by overnight incubation at room temperature. A total of 1 μL of the final bioconjugate solution

Scheme 1. Preparation of ZnO Microrings and Their Conversion into Active Microcontainers for Micro-Raman Spectroscopy[a]

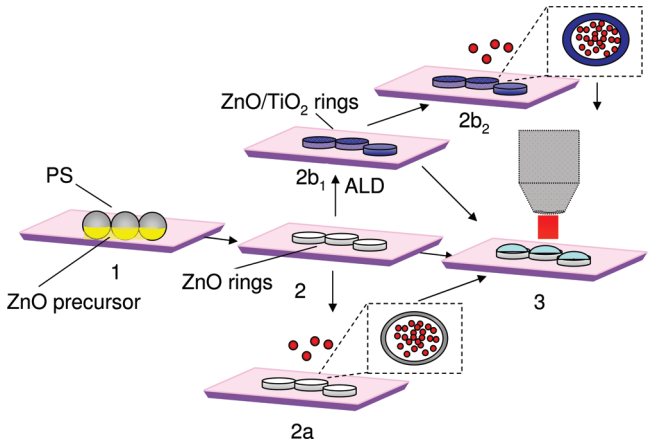

[a] PS assemblies were infiltrated by the ZnO precursor (zinc acetate, 0.05 M in ethanol; step 1). The substrate was transferred onto the hot plate of a heating stage kept at 450°C, and ZnO microrings were generated by fast decomposition of the templates (step 2). These structures were used as femtoliter containers for crystallization of L-glutathione from an aqueous solution. The resulting crystals were analyzed by micro-Raman spectroscopy (step 3). Alternatively, the ZnO microrings were made SERS-active femtoliter containers through the deposition of metal nanoparticles (step 2a). This configuration was employed for the micro-Raman analysis of YCc reported in the text. These structures can be tested also as scaffolds for the deposition of other metal and metal oxide thin layers (step $2b_1$). In the present case, ZnO/TiO_2 heterostructures were achieved by ALD of a thin layer of TiO_2. These heterostructures were used for the testing of photoinduced reactions in a Au-conjugated MB solution (steps $2b_2$ and 3).

was dropped onto a ZnO microring substrate and dried in air at room temperature. Spectra were acquired by focusing the laser through a 100× objective (NA 0.9) into different rings for 60 s.

For the photoinduced SERS experiments, we incubated a 10^{-4} M solution (pH = 6.9) of methylene blue (MB, $C_{16}H_{18}N_3SCl$) with the same Au NPs as those used for previous SERS experiments and then we dropped 1 μL of this solution onto the ZnO/TiO_2 microrings deposited onto a silicon substrate. SERS detection of MB was carried out with a 100× microscope objective (NA 0.9) for 5 s. The photocatalytic degradation experiments were performed by dropping 1 μL of the Au-conjugated MB solution onto the ZnO/TiO_2 microrings and then irradiating the sample with a Philips UV lamp, which emits from 340 to 410 nm, with a peak maximum at 365 nm. The distance between the lamp and the sample was 1 cm. The sample was directly UV-irradiated without moving the Raman stage, to ensure that all of the Raman spectra were acquired exactly in the same zone.

3. RESULTS AND DISCUSSION

Scheme 1 outlines the main steps of the experimental procedure used to prepare ZnO microrings and their subsequent modifications. Details are given in the Experimental Section. The ZnO liquid precursor is infiltrated into a substrate previously coated with PS microspheres (step 1). The substrate is transferred to the hot plate of a heating stage that had been previously heated at 450 °C (step 2). This step yields ZnO microrings that may be differently modified, depending on their final application. For example, they can be made SERS-active femtoliter containers through the deposition of Au or Ag NPs (step 2a). Alternatively, they can serve as scaffolds for the deposition of other metal and metal oxide thin layers (step $2b_1$). Again, the addition of colloidal nanoparticles or Au-conjugated analytes (step $2b_2$) makes these heterostructures active for SERS-based investigations (step 3).

3.1. Preparation of ZnO Microrings. PS microspheres (diameter 5.46 μm) deposited from water/ethanol suspensions were used as templates for preparing ZnO microrings. The final shape and morphology of the microrings are dictated by the initial pattern of these templates. The PS microspheres may be assembled with different configurations, which range from random clusters (incomplete monolayers) to 3D-ordered multilayers, simply by changing the concentration of the suspension and the solvent evaporation rate (22). In the present case, we were interested in preparing either single-layered chains or complete monolayers of PS spheres on glass and silicon substrates; therefore, we started from highly diluted suspensions (see the experimental details).

After drying, the PS layer was heated for 30 s at 125 °C to improve the interconnection between the spheres and their adhesion to the substrate (23). In fact, polymer beads such as PS or poly(methyl methacrylate) (PMMA) exhibit glass transition at a relatively low temperature ($T_g \sim 110-120$ °C) because of the free-volume change between the polymer chains. Thus, the interstices can be reduced in size by heating slightly above the T_g of the polymer colloidal masks. This mechanical stabilization prevents the spheres from being separated during infiltration of the precursors, which was carried out by soaking the substrates in a zinc acetate solution for 2 h (see Figure S1 in the Supporting Information). The formation of ZnO microrings was obtained by putting the infiltrated substrates on a hot plate, which had been heated at 450 °C. This is a key preparatory step. The PS spheres burned (flash point 345−360 °C; self-ignition temperature ~427 °C) and zinc acetate abruptly decomposed (decomposition temperature 237 °C), giving rise to ZnO microrings. These processes occurred immediately, so that ring-shaped microwells, 2−4 μm in diameter, could be achieved in a few seconds. Further heating at this temperature for a few hours may be carried out when final applications call for ZnO microrings with improved crystallinity, as shown in Figure S2 in the Supporting Information. Figure 1a shows a typical SEM image of the necklace-shaped rings generated from random PS assemblies and abruptly heated at 450 °C for 1 h. A more representative overview of the sample morphology was provided by a lower magnification image displayed in Figure S4a in theSupporting Information. Full monolayered structures yielded inverse opal networks (Figure S4b in the Supporting Information). Thanks to the preliminary stabilization, the original PS templates were interconnected with each other, forming long chains ubiquitously distributed all over the sample surface, with no significant differences between glass and silicon substrates. In the case of microrings, interconnection mostly depends on the degree of infiltration of the precursor, which depends, in turn, on both the concentration of the precursor solution

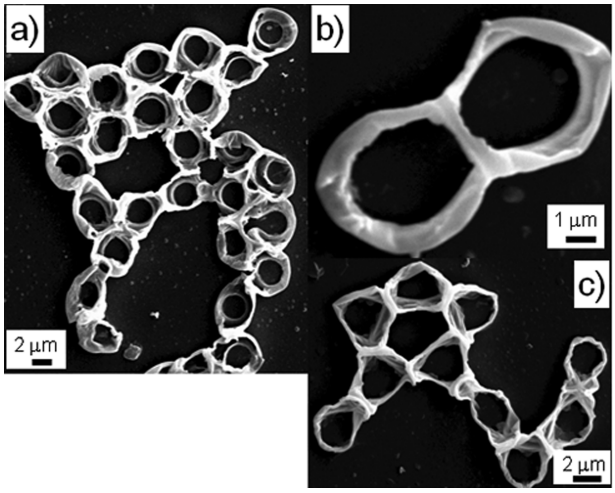

FIGURE 2. SEM images of the ZnO/TiO_2 heterostructures achieved by coating the ZnO rings with TiO_2 (nominal thickness 50 nm) by ALD. (a−c) Examples of interconnected, ring-shaped multimeric structures (see the text for details).

and the wettability of the PS surface. In the present case, a good wettability was ensured by using an ethanol solution of the precursor. When the precursor was able to fill the interstice between the two spheres up to their touching points, the resulting rings were well interconnected with each other. On the other hand, when infiltration was restricted to the sphere cap in direct contact with the substrate, free, "unchained" rings were generated, as shown in Figure 1b. Infiltration influences the final height of the microrings and, ultimately, their volumetric capacity. From SEM and AFM profile analyses (not shown), the height of the ring walls range from 250 to 350 nm, so that the maximum volume capacity is less than 5 fL.

The rapid burning of close-packed agglomerates of PS microspheres yielded hierarchically organized rings with complex multimeric shapes, such as those shown in Figure 2c,d. As we mentioned above, the rapid combustion synthesis is a key step for getting ZnO rings. Although the overall process deserves further characterization, which is currently underway, some important observations should be pointed out. First, the rings cannot be produced by slow heating of the substrate starting from room temperature. Indeed, when the temperature exceeds that of the PS glass transition, the templates lose their spherical shape and a continuous polymeric film blending zinc acetate expands all over the substrate. Moreover, zinc acetate decomposition occurs approximately 200 °C below the onset of PS degradation, so that a slow heating process would have a detrimental effect for the ZnO walls. Second, as shown in Figure S5 in the Supporting Information, a direct burning at 450 °C of noninfiltrated PS microspheres did not allow the ring shapes to be retained, apart from a few sporadic ultraflat polymeric footprints coming from preliminary thermal stabilization. Most of the polymer was burnt after a few seconds, and the remaining part formed a disordered network of aggregates. This means that the zinc precursor is essential for preparing the rings. Indeed, PS and zinc acetate play a synergic role. Part of the heat produced by the exothermic decomposition of PS is exploited to boost ZnO crystallization and, at the same time, the interaction between PS and zinc acetate promotes a binding effect, which allows for robust, ring-shaped structures to be created. This procedure allowed one to obtain a variety of ZnO structures based on ringlike shapes with no need to remove the PS templates by RIE, which is usually employed in the preparation of analogous samples (7, 9).

A further important advantage, in view of spectroscopic analysis, is that the ring(s) to be used for carrying out an experiment can be precisely selected by direct, preliminary inspection with an optical microscope. Thus, control of the morphology can be restricted only to a very local level and does not have to be extended over large scales. This allows one to overcome the intrinsic defectiveness associated with the use of PS spheres as lithographic templates and converts potential drawbacks, such as the ZnO morphological variability coming from nonuniform heat propagation and transfer, occurring during the explosive process, into novel opportunities. Indeed, the production of microcontainers with a large variety of morphologies in a single batch could be exploited for different kinds of experiments onto a single substrate.

3.2. ZnO/TiO_2 Rings. Microrings can be exploited as scaffolds for the deposition of functional metal oxides, giving rise to heterostructured architectures. For example, we recently demonstrated that CeO_2/TiO_2 inverse opals can be suitable for photocatalysis and related applications (10). Here the ZnO microrings were coated with a 50-nm-thick layer of TiO_2 by ALD, following the procedure that we used in our previous work (10). This technique was chosen because it allows for excellent control of the deposited layer thickness and, most importantly, because it can yield very conformal depositions (24). In the present case, the deposition process allowed the original shape of the rings to be fully preserved, as is illustrated in Figure 2. Thus, the coating layer perfectly fitted the complex morphology of the rings. These types of conformal coatings can be exploited as a compact barrier for protecting ZnO from dissolution when the subsequent analytical protocol requires operation under strong acid or basic conditions. In fact, although very recently Knez et al. (25) demonstrated that the ZnO/ TiO_2 interface is actually instable, the effects of such an instability appear only after 3 weeks. Thus, within this period, these heterostructured samples can be used for analytical purposes. Moreover, this potential drawback should not appear when ZnO rings are coated by other oxides, such as Al_2O_3. In addition, effective control of the final thickness of the TiO_2 layer may be obtained by changing the number of ALD cycles. This is an important option for the design of metal oxide photocatalysts. In fact, the thickness of the oxide layer that is active in many photocatalytic processes can be less than 100 nm. A careful optimization of the photoactive layer is necessary to avoid the useless consumption of materials, as well as to improve the efficiency of these processes. Analogous arguments may be applied for the case of oxides used as photoelectrodes for dye-sensitized solar cells, such as the

electron−hole charge separation length is limited to a few nanometers and the efficiency of thicker electrodes can be strongly affected by charge trapping. Moreover, controlling the thickness of the overlayer can be an easy way to tune the volume of containers achieved from smaller scaffolds, allowing one to reach atto- and zeptoliter volumes.

The as-deposited layer was annealed in air at 450 °C for 3 h to convert the amorphous titania into anatase, as shown by the XRD pattern of the TiO_2/ZnO microrings after annealing reported Figure S3 in the Supporting Information. The grain size of anatase, roughly estimated from Debye−Scherrer's equation for the (101) reflection (25.3°), was 23 nm. On the other hand, the value estimated for ZnO from the (100) reflection (31.6°) was 13.5 nm. This large difference in size of coherent diffraction domains mainly depended on the annealing temperature, which was kept quite low in order to avoid the conversion of anatase into rutile. At the same time, the low annealing temperature prevented the formation of a TiO_2/ZnO mixed phase (e.g., $ZnTiO_3$ and Zn_2TiO_4), which can be achieved only above 600 °C.

Similar approaches can be extended to achieve other functional oxide overlayers, such as Al_2O_3 or SiO_2, providing a versatile approach, which can be addressed to a number of in situ experiments.

3.3. Proof-of-Concept Experiments. Different proof-of-concept experiments were designed to check the capabilities of ZnO microrings and ZnO/TiO_2 heterostructures. ZnO microrings were used as microcontainers to crystallize small amounts of L-glutathione within specific areas, which can be directly analyzed by micro-Raman spectroscopy. They were also exploited for the SERS investigation of a model redox protein (YCc). Finally, heterostructured rings were employed as SERS-active microwells for an in situ monitoring of different photoreactions. All of these experiments took advantage of coupling with optical microscopy, which enables one to inspect specific rings and differently shaped compartments. Thus, regions containing higher amounts of analyte can be directly selected and preconcentration effects may be fully exploited.

Finally, one of the most important features of all of these microring-based assays is that the probing laser can be confined either within or onto the ring walls, allowing precise spatial control of the analyzed region (see Figure S6 in the Supporting Information).

3.3.1. In Situ Crystallization of L-Gluta-thione. Glutathione (γ-glutamylcysteinylglycine) is a tripeptide that plays a key role in intracellular metabolism (Figure 3). Inside cells it exists in both reduced (GSH) and oxidized (GSSG) forms, with a constant ratio (about 10) between GSH/GSSG, which is controlled by glutathione disulfide reductase. Glutathione is active against oxidative damage and is directly involved in detoxification and drug resistance. Monitoring of the glutathione levels is important in the study of Alzheimer's and Parkinson's diseases (26), as well as for cancer diagnostics (27). Moreover, it has been used in nanotechnology to synthesize extended networks of noble-metal nanoparticles (28). However, Raman detection of glutathione

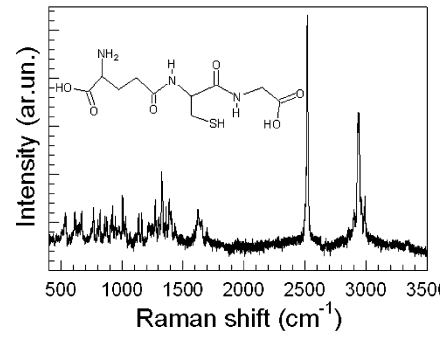

FIGURE 3. Micro-Raman spectrum of L-glutathione (sketched on the top) crystals grown into the ZnO microrings.

and the study of its interactions with drugs or other biologically relevant molecules are quite irksome because of its low cross section (29). Sensitivity can be significantly enhanced by SERS-based methods. On the other hand, these approaches provide for the direct conjugation of glutathione with Au or Ag NPs, which is obtained either through covalent bonding between metal nanoparticles and the thiol group or by adsorption of carboxylic termination. This may alter the reactivity of glutathione, thus preventing a subsequent reliable characterization of its interactions with other molecules. A promising way to bypass these limitations relies on concentrating glutathione into specific compartments, which can eventually serve as analytical platforms for subsequent experiments. Here we took advantage of the ZnO microrings as small containers to entrap glutathione microcrystals.

Micron- and submicrometer-sized crystals of L-glutathione were grown through a laser-assisted slow evaporation of initially saturated water solutions dropped onto the microrings, which was followed by a prolonged annealing at 115 °C to remove residual water (see Figure S7 in the Supporting Information). Improvements in spatial localization could be obtained by a dip-pen-based approach, as well as by nanopipetting. A typical Raman spectrum of these crystals is shown in Figure 3. The most intense peak, located at 2524 cm^{-1}, is assigned to the −SH mode of the cysteinyl group. This indicated that glutathione crystals are in the reduced form (GSH), and no oxidation occurred during deposition and crystallization steps. Other strong peaks grouped in the 2850−3000 cm^{-1} range come from $-CH_2$ stretching, while weak broad signals in the 3000−3400 cm^{-1} region are due to stretching of −NH, which might be detected more clearly with IR spectroscopy. The spectral region ranging from 1490 to 1710 cm^{-1} contains signals of amides I and II. In particular, the signal at 1707 cm^{-1} is ascribed to the C═O stretching, and its spectral position indicates that carbonyl was hydrogen-bonded (30). The signals at 1660 and 1630 cm^{-1} are amide I modes (different −CO and −CN stretches and deformations). Very weak signals in the 1490−1615 cm^{-1} region are attributed to amide II (−NH + CN, at about 1560 and 1537 cm^{-1}) and to $-NH_3^+$ bands (1492 cm^{-1}). The symmetrical COO^- mode of the glutamyl residue appears in the intense peaks around 1400 cm^{-1}, and amide III modes are found in the region between 1230 and 1350 cm^{-1}. The remaining part of the

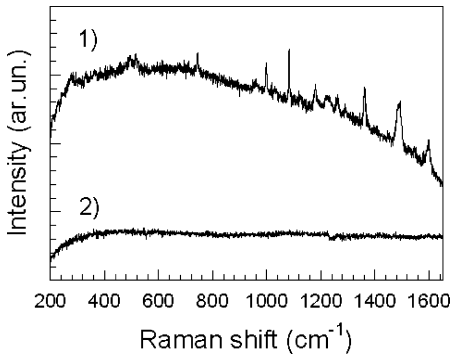

FIGURE 4. (1) Micro-Raman spectrum of Au-conjugated YCc deposited into ZnO microrings. (2) Spectrum of a nonconjugated YCc acquired under the same conditions.

spectrum contains signals of amide IV and V modes, as well as those of skeletal stretches and deformations. The CS stretching mode of the cysteinyl residue appeared at 667 cm^{-1}, partially overlapped with an amide V mode. A more detailed analysis of the Raman modes (30) suggests that the glutamyl-peptidic C═O is involved in intermolecular hydrogen bonding with carboxylate groups and that the cysteinyl-peptidic NH is intramolecularly hydrogen-bonded with the glutamyl COO^-. On the other hand, the cysteinyl-peptidic C═O is intermolecularly bonded to $-NH_3^+$ groups, whereas the glycyl-peptidic NH makes hydrogen bonds with carboxylates. These results are in agreement with those reported by Qian and Krimm (31) and demonstrated that native, fully active crystals of glutathione can be grown and characterized in the ZnO microrings and that these systems can serve for further in situ monitoring of glutathione interaction with other reagents. Although, in this case, the ZnO microrings acted only as physical containers for crystal growth, in many other cases, such as oligonucletide detection (32) or charge-transfer reactions (33), they may play an active role, opening interesting perspectives for a variety of investigations.

3.3.2. SERS Detection of YCc. The capability of ZnO microrings to serve as SERS-active microwells was tested in the detection of YCc. Cytochromes are heme proteins that take part in most of the electron-transfer processes of the mitochondrial respiratory chain, contributing to the stepwise reduction of oxygen and shuttling iron between Fe^{II} and Fe^{III} at the active site. In particular, cytochromes *c* are involved in electron transfer between complexes III (coenzyme Q: cytochrome *c* reductase) and IV (cytochrome *c* oxidase). Cytochromes *c* are characterized by an iron porphyrin group covalently bound to the protein matrix through thioether linkages involving two cysteine residues (Cys14 and Cys17). In addition to this common structure, YCc is provided with an extra cysteine (Cys 102), which can be used for direct conjugation with metals through sulfur termination (34). In the present case, YCc was previously incubated in a Au NP colloidal suspension for 2 h, then dropped onto the microrings, and dried. Direct inspection by means of an optical microscope coupled to a Raman spectrophotometer allowed for the selection of microrings containing the highest concentration of bioconjugates.

Figure 4 shows a typical spectrum of Au-conjugated YCc (1) compared to that achieved from native, nonconjugated YCc (2), which was acquired under the same conditions. In the latter case, none of the YCc modes was detected, indicating that gold conjugation actually yielded a surface enhancement effect.

The Raman spectra of cytochrome *c* are strongly featured by vibrations of the heme ring. A detailed analysis of the local coordinates of porphyrin vibrational modes can be found in work reported by Spiro et al. (35) We just recall that modes classified as ν_{15} (pyr breathing, B_{1g}), ν_4 (pyr half-ring$_{symm}$, A_{1g}), and ν_3 ($C_\alpha C_m$, A_{1g}) are, in general, analyzed to determine spin and oxidation states of the iron in heme rings of cytochrome *c*. In the present case, these oxidation state markers were found at 746, 1360, and 1492 cm^{-1}, respectively. These positions indicate that iron is mainly present in its reduced form (Fe^{2+}). In fact, in the presence of Fe^{3+}, ν_4 and ν_3 modes would have been significantly upshifted (1375 and 1501 cm^{-1}, respectively). These results agree with those found by other groups (34) for YCc solutions, confirming that YCc retained its native configuration. This is important information in view of integrating YCc into biosensors. Moreover, this simple Raman assay can be used for monitoring distortions of the local structure of heme proteins during several redox processes, as well as investigating electron transfer at protein/metal nanoparticle interfaces.

Another important aspect to point out is that, unlike most of the SERS studies on cytochrome *c*, we acquired the spectra with out-of-resonance conditions. Resonant Raman spectra can be obtained by exciting YCc at 514 or 532 nm, which correspond to β or Q bands characteristic of heme electronic transitions. This strongly improves sensitivity to the iron porphyrin ring stretching vibrations. On the other hand, such a strong enhancement of the heme bands leads to an almost complete overwhelming of the amino acid bands, which have a lower Raman cross section and absorb in UV. Thus, in resonant Raman spectra, the amino acid signals are, in general, lacking or very weak (36). This can represent a severe limitation when more complete structural information concerning, for example, the orientation of YCc adsorbed on a solid surface, or conjugated with a nanoparticle, is needed. Here, the out-of-resonance conditions enabled us to detect the spectral contributions of amino acids, which can be observed in the 800−1100 cm^{-1} region, where there are no strong iron porphyrin bands.

In addition, some studies reported that the strong absorption of the exciting laser under resonant conditions may disrupt the distal pocket of the heme group (37). On the contrary, in the present case, the spectra were stable and reproducible even after several acquisitions and prolonged irradiation. Thus, this setup represents a promising solution because it allows for a good trade-off among various conflicting aspects associated with the Raman analysis of heme proteins.

Finally, it is important to remark that functional proteins are, in general, quite expensive, and they can be utilized for analysis in very small amounts. Moreover, although detec-

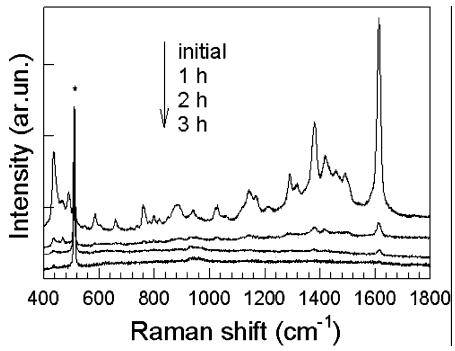

FIGURE 5. SERRS spectra of MB adsorbed onto ZnO/TiO_2 heterostructures before and after UV irradiation (see the text for details). The silicon substrate is indicated by an asterisk.

tion techniques have made giant progress in the last years, many limitations exist for analytical tools capable of monitoring processes and mimicking biological reactions in vitro.

Thus, SERS-active microwells can represent suitable tools for the spectroscopic detection and analysis of functional proteins.

3.3.3. Photocatalytic Experiments. The last series of experiments was focused on testing the ZnO/TiO_2 heterostructured microrings for promoting and monitoring photoinduced reactions. As a first step, the SERS activity of these systems was tested in the detection of MB. MB is commonly used as a Raman probe molecule because it adsorbs onto gold surfaces, shows little fluorescence background, and represents a good model for azo-dye compounds. Moreover, it is intensively investigated in pharmacology and photodynamic therapy for the selective destruction of cancerous cells, bacteria, viruses, etc. (38). We incubated a 10^{-4} M MB solution with the same Au NPs as those used for previous SERS experiments, and then we dropped 1 μL of this solution onto the ZnO/TiO_2 microrings deposited onto a silicon substrate. Micro-Raman spectra were acquired after drying, having tuned the laser at low power (0.5 mW) in order to avoid possible photobleaching of the dye. The Raman spectra of MB exhibited strong signals all over the frequency range, in spite of the low concentration of the analyte and short acquisition time (5 s; see the initial spectrum in Figure 5). On the other hand, MB deposited with the same concentration onto bare silicon substrates did not show any detectable signals when acquired under the same conditions. Thus, a surface enhancement induced by MB adsorption onto the Au NPs was achieved. More precisely, because the main absorption band of MB falls within the frequency range of excitation, the surface-enhanced Raman measurements were carried out under resonant conditions (SERRS). This benefit can be exploited to investigate photoinduced reactions occurring in these heterostructured microwells. For example, MB photodegradation under UV irradiation was monitored in situ by coupling the micro-Raman stage with a lamp emitting in the 340−410 nm range (Figure 5). The initial spectrum exhibited all of the Raman signals of MB, which were strongly enhanced by SERR conditions, as discussed above. The intensity of the MB peaks decreased progressively upon UV irradiation. After 3 h, even the most intense signal of MB (the C−C ring

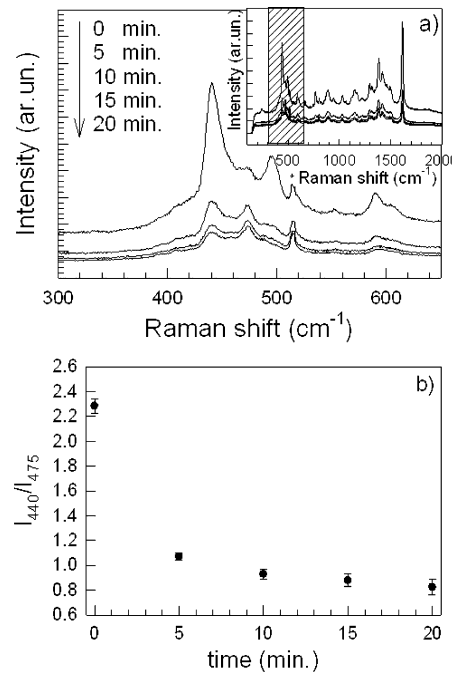

FIGURE 6. (a) Plasmonic heating effects induced by laser irradiation. The spectral region used for monitoring the conversion of MB dimers into monomers is highlighted in the inset and expanded in the main figure. The silicon substrate is indicated by an asterisk. The plot of MB upon irradiation for 20 min overlaps the 15 min plot and has been omitted for clarity. (b) Intensity ratio between the Raman modes at about 440 and 475 cm^{-1}, which are characteristic of the aggregated and monomeric species, respectively, as a function of the laser irradiation time.

stretching, located at 1618 cm^{-1}) was below the detection limit, indicating that the photodegradation process occurred almost completely. Thus, as was already reported in our previous studies and in agreement with the literature (10, 39), less than 50-nm-thick layers of TiO_2 can be active enough to get good photocatalytic performances.

In a second experiment, we tested the heating effects induced by laser irradiation in MB adsorbed onto Au NPs. Indeed, upon adsorption, MB tends to form dimers or aggregated species. The conversion of MB dimers into monomers is an endothermic process that can be promoted by heat generated upon light absorption (40). Although here excitation takes place under resonant conditions, this conversion did not occur when a reference MB sample was irradiated under the same conditions as those used for this experiment (laser power 0.05 mW). On the contrary, the presence of metals might promote this effect even at low power density. To check this conversion and evaluate its progress, the Raman spectra were acquired by repeating the same measurement at the same point, every 5 min. Whole spectra are displayed in the inset of Figure 6a. We focused on the region between 400 and 600 cm^{-1}, which contains information on both dimeric and monomeric species (Figure 6a). In particular, the Raman mode at about 475 cm^{-1} is ascribed to the thiazine ring in-plane bending mode of MB adsorbed as a monomer, whereas other skeletal C−N−C bending modes at 450 and 502 cm^{-1} are associated with dimers or aggregates (40). In the first acquisition, the signal at 475 cm^{-1} was quite weak, whereas modes at 450 and 502

cm^{-1} were strong, indicating that MB molecules were mainly adsorbed as dimeric species or aggregates. Upon irradiation for 5 min, the signal of the monomer became stronger, whereas the signals of aggregated species decreased in their intensity, indicating that part of the MB dimers had been converted into monomers. This process continued in the subsequent steps and stopped after 20 min. The intensity ratios of the peaks at 450 and 475 cm^{-1} as a function of the irradiation time are plotted in Figure 6b. This change of the intensity ratio goes along with a general decrease of the spectral intensity of the MB bands, as can be observed from the ever-decreasing baseline and from the increase of the substrate peak, which can be taken as an internal reference. This result suggests that laser irradiation induced photodesorption of part of MB. Because these processes did not occur when MB alone was irradiated under the same conditions, we may argue that these effects are promoted by the presence of Au NPs. We have already demonstrated that Au NPs act as very efficient photothermal converters, and this efficiency is high enough to cause heat-driven processes, even at low power excitations (19–21). On the other hand, the effects observed in the present case are weaker than the effects that we recently reported for laser irradiation of Au/TiO_2 nanocomposites (41). This can be explained considering that, in the latter case, the Au NPs were densely aggregated in nanoshell architectures that maximized the optothermal conversion, whereas in the present case, the Au NPs used to confer SERS activity to the ZnO/ TiO_2 microwells are only physically adsorbed onto the anatase surface in the form of random aggregates, so that they cannot take full advantage of collective effects to enhance their conversion efficiency.

Similar investigations can be extended to a number of surface processes and represent an important diagnostic tool for the newborn field of plasmonic photocatalysis, which seeks to combine the photocatalytic properties of some oxides, such as TiO_2, with the electromagnetic field enhancement occurring in the presence of metal nanoparticles, in order to boost the efficiency of some reactions (42). Moreover, this simple assay may allow for the optimization of important parameters such as the thickness of the photocatalytic layer and could be conveniently used to test the degradation of toxic pollutants or dangerous reactions, in which working with very small amounts of chemicals is mandatory.

4. CONCLUSIONS

This work demonstrated that ZnO microrings and ZnO/TiO_2 heterostructures can be easily generated and converted into SERS-active microcontainers with volume capacities on the order of femtoliters, which can be addressed to a variety of spectroscopic experiments involving, for example, biomolecules, proteins, and organic pollutants. The fabrication is based on the fast degradation of precursor-infiltrated PS templates and allows the yield of necklace rings, hierarchical assemblies, or inverse opal networks depending on both the geometrical arrangement of the templates and the volume of the infiltrated precursor. Starting from these scaffolds, core−shell heterostructures were produced by ALD, taking advantage of good conformality and control of the thickness of the shell layer.

A similar approach may be extended to other functional oxides as well as to smaller volumes, thanks to the wide range of precursors and template sizes (see Figure S8 in the Supporting Information). Far from being competitive with microarray technology for detection purposes or high-throughput parallel screening, this strategy aims to represent a versatile tool for in situ spectroscopic characterization of reactions and processes that cannot be easily monitored by other approaches, and it can be particularly suitable for basic studies requiring high spatial compartmentalization and resolution at one time. Moreover, these types of microcontainers could be conveniently exploited for investigating in vitro laser-induced processes occurring in plasmonic nanoheaters proposed for photothermal therapy. Further advances could be reached either by restricting the amount of analyte to some specific rings, using, for example, nanopipetting or dip-pen-based techniques, or by engineering the rings to achieve superhydrophobic and superhydrophilic sites. This could open challenging perspectives for exploiting the semiconducting character of some transition-metal oxides in order to develop new strategies for the transduction of chemical and biochemical events, aiming to integrate these systems into advanced smart devices.

Acknowledgment. Alessandro Rivetti, Marcello Zucca, and Stefania Federici are acknowledged for assistance with SEM, ALD, and AFM, respectively. This work was supported by Fondazione Cariplo.

Supporting Information Available: Optical microscopic images of PS microspheres before and after infiltration, 2D XRD patterns of the ZnO and ZnO/TiO_2 microrings, SEM and optical images of microrings, and Raman spectra of L-glutathione before and after thermal treatment. This material is available free of charge via the Internet at http://pubs.acs.org.

REFERENCES AND NOTES

(1) (a) Rondelez, Y.; Tresset, G.; Tabata, K. V.; Arata, H.; Fujita, H.; Takeuchi, S.; Noji, H. *Nat. Biotechnol.* **2005**, *23*, 361–365.
(2) Barton, J. E.; Odom, T. W. *Nano Lett.* **2004**, *4*, 1525–1528.
(3) Wang, L.; Min, H. L.; Barton, J. E.; Hughes, L.; Odom, T. W. *J. Am. Chem. Soc.* **2008**, *130*, 2142–2143.
(4) Lam, K. S.; Renil, M. *Curr. Opin. Chem. Biol.* **2002**, *6*, 353–358.
(5) Ostuni, E.; Chen, C. S.; Ingber, D. E.; Whitesides, G. M. *Langmuir* **2001**, *17*, 2828–2834.
(6) Khan, F.; Zhang, R.; Unciti-Broceta, A.; Diaz-Mochon, J. J.; Bradley, M. *Adv. Mater.* **2007**, *19*, 3524–3528.
(7) Yang, S. M.; Jang, S. G.; Choi, D. G.; Kim, S.; Yu, H. K. *Small* **2006**, *2*, 458–475.
(8) Yan, F.; Goedel, W. A. *Angew. Chem., Int. Ed.* **2005**, *44*, 2084–2088.
(9) Sun, Z.; Li, Y.; Zhang, J.; Li, Y.; Zhao, Z.; Zhang, K.; Zhang, G.; Guo, J.; Yang, B. *Adv. Funct. Mater.* **2008**, *18*, 4036–4042.
(10) Alessandri, I.; Zucca, M.; Ferroni, M.; Bontempi, E.; Depero, L. E. *Small* **2009**, *5*, 336–340.
(11) Alessandri, I.; Bergese, P.; Depero, L. E. *J. Nanosci. Nanotechnol.* **2009**, *9*, 1597–1602.
(12) Ljosa, V.; Carpenter, A. E. *Trends Biotechnol.* **2008**, *26*, 527–530.
(13) Weckhuysen, B. M. *Angew. Chem., Int. Ed.* **2009**, *48*, 4910–4943.
(14) Aroca R. *Surface-Enhanced Vibrational Spectroscopy*; Wiley: Chichester, U.K., 2006.
(15) Kneipp, K.; Wang, Y.; Kneipp, H.; Perelman, L. T.; Itzkan, I.; Dasari, R.; Feld, M. S. *Phys. Rev. Lett.* **1997**, *78*, 1667.

(16) Bhuvana, T.; Kulkarni, G. U. *Nanotechnology* **2009**, *20*, 045504.
(17) Zamuner, M.; Talaga, D.; Deiss, F.; Guieu, V.; Kuhn, A.; Ugo, P.; Sojic, N. *Adv. Funct. Mater.* **2009**, *19*, 3129–3135.
(18) Ko, H.; Tsukruk, V. V. *Small* **2008**, *4*, 1980–1984.
(19) Alessandri, I.; Depero, L. E. *Nanotechnology* **2008**, *19*, 305301.
(20) Alessandri, I.; Ferroni, M.; Depero, L. E. *ChemPhysChem* **2009**, *10*, 1017–1022.
(21) Alessandri, I.; Depero, L. E. *Chem. Commun.* **2009**, *17*, 2359–2361.
(22) Velev, O. D.; Gupta, S. *Adv. Mater.* **2009**, *21*, 1897–1905.
(23) (a) Blanford, C. F.; Yan, H.; Schroden, R. C.; Al-Dous, M.; Stein, A. *Adv. Mater.* **2001**, *13*, 401–407. (b) Stein, A.; Li, F.; Denny, N. R. *Chem. Mater.* **2008**, *20*, 649–666.
(24) Knez, M.; Nielsch, K.; Niinistö, L. *Adv. Mater.* **2007**, *19*, 3425–3438.
(25) Yang, Y.; Kim, D. S.; Qin, Y.; Berger, A.; Scholz, R.; Kim, H.; Knez, M.; Gösele, U. *J. Am. Chem. Soc.* **2009**, *131*, 13920–13921.
(26) Miller, V. M.; Lawrence, D. A.; Mondal, T. K.; Seegal, R. F. *Brain Res.* **2009**, *1276*, 22–30.
(27) Bredel, M. *Brain Res. Rev.* **2001**, *35*, 161–204.
(28) Duan, X. R.; Li, Z. P.; Cui, P. J.; Su, Y. Q. *J. Nanosci. Nanotechnol.* **2006**, *6*, 3842–3848.
(29) Huang, G. G.; Han, X. X.; Hossain, M. K.; Ozaki, Y. *Anal. Chem.* **2009**, *81*, 5881–5888.
(30) Picquart, M.; Grajcar, L.; Baron, M. H.; Abedinzadeh, Z. *Biospectroscopy* **1999**, *5*, 328–337.
(31) Qian, W.; Krimm, S. *Biopolymers* **1994**, *34*, 1377–1394.
(32) (a) Kumar, N.; Dorfman, A.; Hahm, J. *Nanotechnology* **2006**, *17*, 2875–2881. (b) Liu, Y.; Zhong, M. Y.; Shan, G.; Li, Y.; Huang, B.; Yang, G. *J. Phys. Chem. B* **2008**, *112*, 6484–6489.
(33) Yang, L.; Ruan, W.; Jiang, X.; Zhao, B.; Xu, W.; Lombardi, J. R. *J. Phys. Chem. C* **2009**, *113*, 117–120.
(34) Delfino, I.; Bizzarri, A. R.; Cannistraro, S. *Biophys. Chem.* **2005**, *113*, 41–51.
(35) (a) Li, X.-Y.; Czernuszewicz, R. S.; Kincaid, J. R.; Su, O. Y.; Spiro, T. G. *J. Phys. Chem.* **1990**, *94*, 31–47. (b) Li, X.-Y.; Czernuszewicz, R. S.; Kincaid, J. R.; Stein, P.; Spiro, T. G. *J. Phys. Chem.* **1990**, *94*, 47–61.
(36) Yeo, B.-S.; Mädler, S.; Schmid, T.; Zhang, W.; Zenobi, R. *J. Phys. Chem. C* **2008**, *112*, 4867–4873.
(37) Feng, M.; Tachikawa, H. *J. Am. Chem. Soc.* **2008**, *130*, 7443–7448.
(38) Tang, W.; Xu, H.; Kopelman, R.; Philbert, M. A. *Photochem. Photobiol.* **2005**, *81*, 242–249.
(39) Mills, A.; Elliott, N.; Parkin, I. P.; O'Neill, S. A.; Clark, R. J. H. *J. Photochem. Photobiol. A: Chem.* **2002**, *151*, 171–179.
(40) Nicolai, S. H. A.; Rubim, J. C. *Langmuir* **2003**, *19*, 4291–4294.
(41) Alessandri, I.; Ferroni, M. *J. Mater. Chem.* **2009**, *19*, 7990–7994.
(42) Awazu, K.; Fujimaki, M.; Rockstuhl, C.; Tominaga, J.; Murukami, H.; Ohki, Y.; Yoshida, N.; Watanabe, T. *J. Am. Chem. Soc.* **2008**, *130*, 1676–1680.

AM900904K